

# Hilltop Curvature Increases with the Square Root of Erosion Rate

E. J. Gabet<sup>1</sup>, S. M. Mudd<sup>2</sup>, R. W. Wood<sup>1</sup>, S. W. D. Grieve<sup>3</sup>, S. A. Binnie<sup>4</sup>, T. J. Dunai<sup>4</sup>

<sup>1</sup> Department of Geology, San Jose State University, San Jose, California, 95192, USA.

<sup>2</sup> School of Geosciences, University of Edinburgh, Edinburgh, UK, EH9 3FE.

<sup>3</sup> School of Geography, Queen Mary University of London, London, UK, E1 4NS.

<sup>4</sup> Institute for Geology and Mineralogy, University of Cologne, Germany, 50674.

Corresponding author: Emmanuel Gabet (manny.gabet@sjsu.edu)

## Key Points:

- Hilltop curvature at our sites does not vary linearly with erosion rate, as predicted by theory
- The inferred transport coefficient appears to be insensitive to climate
- Processes affecting the underlying bedrock may control the shape of soil-mantled hillslopes

## Abstract

The shape of soil-mantled hillslopes is typically attributed to erosion rate and the transport efficiency of the various processes that contribute to soil creep. While climate is generally hypothesized to have an important influence on soil creep rates, a lack of uniformity in the measurement of transport efficiency has been an obstacle to evaluating the controls on this important landscape parameter. We addressed this problem by compiling a data set in which the transport efficiency has been calculated using a single method, the analysis of hilltop curvatures using 1-m LiDAR data, and the erosion rates have also been determined via a single method, *in-situ* cosmogenic <sup>10</sup>Be concentrations. Moreover, to control for lithology, we chose sites that are only underlain by resistant bedrock. The sites span a range of erosion rates (6 – 922 mm/kyr), mean annual precipitation (39 – 320 cm/yr), and aridity index (0.08 – 1.38). Surprisingly, we find that hilltop curvature varies with the square root of erosion rate,

31 whereas previous studies predict a linear relationship. In addition, we find that the inferred  
32 transport coefficient also varies with the square root of erosion rate but is insensitive to  
33 climate. We explore various mechanisms that might link the transport coefficient to the  
34 erosion rate and conclude that present theory regarding soil-mantled hillslopes is unable to  
35 explain our results and is, therefore, incomplete. Finally, we tentatively suggest that  
36 processes occurring in the bedrock (e.g., fracture generation) may play a role in the shape of  
37 hillslope profiles at our sites.

38 **Index Terms: 1826, 1819, 1862**

### 39 **1. Introduction**

40 On soil-mantled surfaces too gentle for significant landsliding, particles are primarily  
41 transported downslope by soil creep. Soil creep is a general term for the cumulative effect of  
42 myriad individual processes that locally disturb soil, such as the freezing and thawing of pore  
43 water [Anderson *et al.*, 2013], shrink-swell cycles [Carson and Kirkby, 1972], dry ravel  
44 [Anderson *et al.*, 1959; Gabet, 2003], burrowing by animals [Gabet *et al.*, 2003], and tree  
45 throw [e.g., Denny and Goodlett, 1956]. Culling [1963] proposed that the rate of soil creep  
46 ( $q_s$ ; L<sup>2</sup>/T) is linearly proportional to hillslope gradient,  $S$  (L/L), such that

$$47 \quad q_s = DS \quad (1)$$

48 where  $D$  (L<sup>2</sup>/T) is a sediment transport coefficient. The sediment transport coefficient,  $D$ , is a  
49 measure of the efficiency of the various soil creep processes, and its magnitude sets the pace  
50 for hillslope evolution [e.g., Fernandes and Dietrich, 1997; Roering *et al.*, 1999]. Although a  
51 nonlinear relationship between gradient and flux is supported by topographic analysis  
52 [Andrews and Bucknam, 1987; Grieve *et al.*, 2016; Hurst *et al.*, 2012; Roering *et al.*, 1999]

53 and physical simulations [Gabet, 2003; Roering et al., 2001b], this relationship reduces to  
54 Eqn. (1) on slopes  $< 20^\circ$  [Hurst et al., 2012].

55 Our understanding of the controls on  $D$  for a particular landscape is limited. Because  
56 soil creep processes are typically climatically controlled, either directly (e.g., freeze-thaw) or  
57 indirectly through climate's effect on the distribution of the biota, temperature and  
58 precipitation are expected to have a dominant role in the transport efficiency of soil creep  
59 [e.g., Dunne et al., 2010; Hanks, 2000; Pelletier et al., 2011]. Indeed, Hurst et al. [2013] and  
60 Richardson et al. [2019] found that  $D$  increases with mean annual precipitation, albeit  
61 weakly; the latter also found that  $D$  increases with the aridity index, which is the ratio  
62 between precipitation and evapotranspiration [Trabucco and Zomer, 2019]. In contrast, Ben-  
63 Asher et al. [2017] concluded that transport efficiency decreases with precipitation, although  
64 this result was based on a small data set. Soil thickness [Furbish et al., 2009; Heimsath et al.,  
65 2005] and soil texture [Furbish et al., 2009], as well as underlying lithology [Hurst et al.,  
66 2013], may also be important factors. A lack of uniformity in measuring  $D$ , however, has  
67 been an obstacle in investigating the effect of these various factors.

68 Determining the controls on the transport coefficient is important for a variety of  
69 reasons. Because many landscapes are soil-mantled, not affected by overland flow, and too  
70 gentle for significant landsliding, Eqn. (1) and its nonlinear counterpart are thought to offer a  
71 complete description (or nearly so) of sediment transport across much of the Earth's surface.  
72 Moreover, assuming steady-state topography, combining Eqn. (1) with a statement of mass  
73 conservation yields

74 
$$C_{HT} = -\frac{E}{D} \left( \frac{\rho_s}{\rho_r} \right) \quad (2)$$

75 where  $E$  is the erosion rate (L/T),  $C_{HT}$  (1/L) is the two-dimensional curvature (i.e., the  
76 Laplacian of elevation) of a hill's ridgecrest, and  $\rho_s$  and  $\rho_r$  are the density (L<sup>3</sup>/T) of soil and  
77 rock, respectively [Roering *et al.*, 2007]. With this equation (and its nonlinear version),  $D$   
78 and  $E$  are both assumed to be independent variables:  $E$  is controlled by the rate at which the  
79 lower boundary is lowered (e.g., via river incision in response to uplift), and  $D$  is controlled  
80 by the intensity of the various soil creep processes. According to this theory, the profile of a  
81 hillslope adjusts itself such that its curvature satisfies Eqn. (2) [Culling, 1963; Gilbert, 1909].  
82 Therefore, understanding the controls on the transport efficiency should provide insight into  
83 hillslope form. In addition, studies have used Eqn. (1) and its nonlinear version to model the  
84 degradation of fault scarps to estimate earthquake recurrence interval [e.g., Hanks and  
85 Schwartz, 1987], and the results are sensitive to the value of the transport coefficient. Finally,  
86 understanding the role of the various factors on  $D$  is important as geologists attempt to infer  
87 erosion rates based on topographic analyses [Hurst *et al.*, 2012].

## 88 **2. Methods**

### 89 2.1. Site selection and descriptions

90 Appropriate sites were limited to watersheds which had both LiDAR and cosmogenic  
91 <sup>10</sup>Be data sets. The <sup>10</sup>Be data came from a global compilation [Harel *et al.*, 2016], and the  
92 associated LiDAR data were acquired from the OpenTopography (<http://opentopo.sdsc.edu>)  
93 and USGS (<https://viewer.nationalmap.gov>) platforms. LiDAR data with spatial resolutions  
94 coarser than 1-m cannot accurately resolve ridgeline curvatures in all settings [Grieve *et al.*,  
95 2016] and so any sites without 1-m resolution data were excluded from the analysis. Because  
96 ridgeline curvatures were used to estimate  $D$  (see below), only watersheds that appeared to  
97 be in topographic steady-state were chosen. For example, watersheds with clear knickpoints

98 or with asymmetrical ridges were avoided, as well as steep watersheds advancing into low-  
99 relief surfaces. Simulations of hillslope evolution suggest that hillslopes with declining  
100 erosion rates adjust so quickly that they are difficult to differentiate from steady state  
101 hillslopes; furthermore, hillslopes experiencing accelerated uplift only preserve the signature  
102 of changing erosion rates for tens of thousands of years [Mudd, 2017]. Therefore, by  
103 avoiding areas with obvious signs of landscape transience, we are less likely to find ridgeline  
104 curvatures reflective of transient conditions. Thirty sites from six regions in the United States  
105 met our criteria: the Olympic Peninsula (WA) [Belmont *et al.*, 2007], the Feather River area  
106 (CA) [Hurst *et al.*, 2012; Riebe *et al.*, 2001; Saucedo and Wagner, 1992], the San Gabriel  
107 Mountains (CA) [DiBiase *et al.*, 2010], Yucaipa Ridge (CA) [Binnie *et al.*, 2007], the Idaho  
108 Plateau (ID) [Wood, 2013], and the Blue Ridge Mountains (VA) [Duxbury, 2009] (Figure 1) .  
109 Some of the regions (e.g., the San Gabriel Mountains) had  $^{10}\text{Be}$  data for sites not covered by  
110 available LiDAR data and, thus, their full data-sets could not be used. Climatic data for these  
111 sites were obtained from the 800-m resolution PRISM model [PRISM, 2014], which provides  
112 recent (1981 – 2010) 30-yr means for annual precipitation (MAP) and annual temperature  
113 (MAT) (Table 1). The aridity index for the sites was determined from Trabuco and Zomer  
114 [2019]. While these data are for the modern climate, we assume that they are representative  
115 (at least in a relative sense) of the climate state over the time-scale of the erosion rates  
116 measured with  $^{10}\text{Be}$  (i.e.,  $10^3$  -  $10^5$  yrs). To control for rock strength, we chose sites underlain  
117 by lithologies known to be resistant to erosion: plutonic and metamorphic bedrock [e.g.,  
118 Gabet, 2020; Hack, 1973] (Table 1).

119 2.2. Erosion rate calculations

120 To ensure a consistent method for calculating erosion rates, they were determined  
121 from  $^{10}\text{Be}$  concentrations in detrital quartz grains (Table 1). For five of the study regions,  
122 published  $^{10}\text{Be}$  concentrations were used to calculate basin-scale erosion rates. For the Idaho  
123 Plateau sites,  $^{10}\text{Be}$  concentrations were measured from soil and fluvial sediment samples  
124 collected for this study (see below). For all six study regions, erosion rates were calculated  
125 from the  $^{10}\text{Be}$  concentrations using a single algorithm [Mudd *et al.*, 2016].

126 A full description of the Idaho Plateau field area can be found in Wood [2013].  
127 Ridgetop and basin-scale denudation rates were determined by measuring cosmogenic  $^{10}\text{Be}$   
128 concentrations in quartz [Brown *et al.*, 1995; Granger *et al.*, 1996]. The ridgetop rates were  
129 determined from soil samples taken from the top 20 cm of the regolith at three sites. For the  
130 basin-scale erosion rates, fluvial sediment was taken from three 1<sup>st</sup>-order streams. Pure quartz  
131 fractions from the crushed and sieved (250-710  $\mu\text{m}$ ) and magnetically separated samples  
132 were obtained using published procedures [Kohl and Nishiizumi, 1992; Mifsud *et al.*, 2013].  
133 ICP-OES analysis of purity was undertaken on splits of the etched quartz. Samples were  
134 spiked with  $\sim 200\ \mu\text{g}$  of a commercial Be carrier (Scharlab Beryllium ICP standard solution)  
135 and prepared as AMS targets at the University of Cologne using a standard sample  
136 preparation method [2015]. The samples were prepared alongside a reagent blank;  $^{10}\text{Be}$   
137 concentrations following blank subtraction are reported in Table 2. Blank corrections are  $<2$   
138 %, except for sample S2, for which the correction is  $<5$  %. Samples were measured on  
139 CologneAMS [Dewald *et al.*, 2013] and normalized to reference standards [2007].  
140 Uncertainties in the concentrations are estimated by propagating the uncertainties of the

141 AMS measurements and mass of Be added during spiking (estimated  $1\sigma$  uncertainty of 1%)  
142 of both the samples and the blank.

143  $^{10}\text{Be}$  concentrations were converted to denudation rates with the CAIRN software  
144 package, which accounts for topographic shielding and snow shielding [Mudd *et al.*, 2016].  
145 We calculated snow shielding by first fitting a bilinear trend in snow water equivalent (SWE)  
146 as a function of elevation based on regional climate data from the National Oceanic and  
147 Atmospheric Association [NOAA, 2016] and following Kirchner *et al.* [2014]. SWE averages  
148 were converted to snow shielding values by assuming that snow reduces production solely by  
149 spallation [Mudd *et al.*, 2016]. Snow shielding is highly uncertain because of the difficulty of  
150 estimating the average SWE over the timescales of  $10^3 - 10^4$  years. We calculated  
151 denudation rates with no snow shielding to assess the sensitivity of denudation rate to snow  
152 thickness and found that, without accounting for snow, denudation rate estimates could be as  
153 much as 15% higher (for sample S3) but, for most samples, the differences were less than  
154 10%. Uncertainties from analytical error and from uncertainties in production scaling and  
155 shielding are presented in Table 1 [Mudd *et al.*, 2016].

### 156 2.3. Transport Coefficient Calculations

157 Direct estimates of the transport efficiency by field measurements of sediment fluxes  
158 over the relevant time and spatial scales across a range of landscapes are impractical. Instead,  
159 along ridgelines, where slopes are gentle and soil creep is well described by Eqn. (1), the  
160 transport coefficient can be calculated by rewriting Eqn. (2) as

$$161 \quad D = - \left( \frac{E}{C_{HT}} \right) \left( \frac{\rho_r}{\rho_s} \right) \quad (3).$$

162 The ratio  $\rho_r/\rho_s$  was assumed to be 2 [Hurst et al., 2012]; this value is probably only  
163 approximately correct for each of our sites and likely varies by  $\pm 25\%$ . Ridgeline curvatures  
164 were calculated from a 1-m LiDAR DEM for each site using a six-term polynomial function  
165 to fit the elevation data within a circular sliding window with a diameter of 14 m. A value of  
166 14 m for the analysis window was chosen based on sensitivity analyses presented in Grieve  
167 et al. [2016] which followed the method for identifying the optimal window diameter  
168 described in Roering et al. [2010] and Hurst et al. [2012].

169 The second derivative of the polynomial function at the window's center is that cell's  
170 two-dimensional curvature. Because topographic noise could produce outliers, the median of  
171 the curvatures along each watershed's ridgeline was used in our analyses [Hurst et al., 2012].  
172 The average slopes ( $\pm 1\sigma$ ) along the ridgelines, determined as the first derivative of the  
173 polynomial function, ranged from  $0.5 \pm 3^\circ$  (Blue Ridge Mtns) to  $9 \pm 6^\circ$  (Yucaipa Ridge),  
174 thereby validating the use of Eqn. (1). Note that, even at the steepest site along Yucaipa  
175 Ridge, nearly 95% of the area analyzed had slopes  $< 20^\circ$ . Finally, an automated procedure  
176 was used to detect the presence of bedrock outcrops along the ridgelines [Milodowski et al.,  
177 2015] to confirm that the sites were mantled with soil. One Yucaipa Ridge site had 75% soil-  
178 cover and the other had 90% soil-cover; the soil-cover at the other sites ranged from 97 to  
179 100%. Observations of Google Earth<sup>TM</sup> imagery supported these estimates.

### 180 2.3 Additional Data

181 The dataset described above was supplemented with data selected from a compilation  
182 presented in Richardson et al. [2019] (Table 1). From this compilation, four sites met our  
183 criteria: the ridgelines were symmetrical, transport coefficients were estimated by analyzing  
184 ridgetop curvatures from 1-m LiDAR data, erosion rates were determined with cosmogenic

185  $^{10}\text{Be}$ , and the soils were derived from resistant lithologies (Table 1). The only difference is  
186 that Richardson et al. used a 15-m window for their curvature analysis whereas our study  
187 used a 14-m window; we consider this difference to be insignificant. With the combined  
188 datasets, the sites represent a range of erosion rates from 6 to 922 mm/kyr, a range of mean  
189 annual precipitation from 39 to 320 cm/yr, a range of mean annual temperature from 2 to 15°  
190 C, and range of aridity index from 0.08 to 1.38 (Table 1).

#### 191 2.4 Correcting for Grid Resolution

192 As erosion rates increase, ridgelines become sharper, which could potentially weaken  
193 the ability to accurately measure curvature given a fixed grid resolution. In particular, this  
194 grid-resolution effect could lead to an increasing underestimate of curvature as ridgelines  
195 sharpen with increasing erosion rates, thereby artificially introducing a positive relationship  
196 between  $D$  and  $E$ . To correct for this potential artefact, we performed an analysis in which we  
197 compared the estimates of the transport efficiency with those from idealized one-dimensional  
198 (1D) hillslopes. We assumed our ridges can be approximated as one-dimensional because  
199 curvature perpendicular to ridgelines far exceeds curvature parallel to our ridgelines.

200 To begin, we solved for the elevation of an idealized 1D hillslope by assuming that a  
201 nonlinear sediment flux law describes sediment transport on our hillslopes [e.g., *Andrews*  
202 *and Bucknam*, 1987; *Roering et al.*, 1999]

$$203 \quad q_s = - \frac{D \frac{\partial z}{\partial x}}{1 - \left( \left| \frac{\partial z}{\partial x} \right| / S_c \right)^2} \quad (4)$$

204 where  $q_s$  is sediment flux ( $\text{m}^2/\text{yr}$ ),  $D$  is the sediment transport coefficient ( $\text{m}^2/\text{yr}$ ),  $z$  is the  
205 surface elevation,  $x$  is a horizontal distance, and  $S_c$  is a critical slope angle. As noted earlier,

206 this equation reduces to Eqn. (1) at gentle slopes. Inserting Eqn. (4) into a statement of mass  
 207 conservation and solving it under steady-state conditions yields an expression for the  
 208 elevation of a hillslope [Roering *et al.*, 2001a]:

$$209 \quad z = -\frac{S_c^2}{2\beta} \left[ \sqrt{D^2 + \left(\frac{2\beta x}{S_c^2}\right)^2} - D \ln \left( \frac{S_c}{2\beta} \sqrt{D^2 + \left(\frac{2\beta x}{S_c^2}\right)^2} + \frac{S_c D}{2\beta} \right) \right] + c \quad (5)$$

210 where  $\beta$  is the ratio between rock and soil density multiplied by the erosion rate  $((\rho_r/\rho_s)*E)$   
 211 and  $c$  is a constant that sets the absolute elevation of the hillslope profile. At the divide ( $x = 0$   
 212 m), the curvature is equal to:

$$213 \quad \left( \frac{d^2 z}{dx^2} \right)_{HT} = -\frac{\beta}{D} \quad (6).$$

214 As described earlier, curvature at each site was measured from gridded 1-m  
 215 topographic data. To mimic this procedure on the synthetic hillslope, we solved Eqn. (5) on a  
 216 grid of points with a spacing of 1 m. Random noise was then imposed on each gridded data  
 217 point from a uniform distribution ranging from -0.1 to 0.1 m, which is a conservative  
 218 estimate of vertical error in typical airborne LiDAR data. As with the real landscapes, a 2<sup>nd</sup>-  
 219 order polynomial equation was fitted across the ridgetop over a 14-m window and the  
 220 curvature was calculated at the center node.

221 However, in any gridded topography, the highest true elevation of the ridge may not  
 222 be located exactly on the grid sampling point. The exact location of the ridge may be offset  
 223 from the highest gridded pixel by up to half a pixel width. In Eqn. (5), the ridge is located at  
 224  $x = 0$  meters, but to account for the possibility that the ridgeline does not correspond to the  
 225 highest pixel, we allowed the gridded points to shift laterally by 0.5 m to produce an offset  
 226 between the center point in the gridded data and the ridgeline.

227 For each study site (Table 1), the values of  $\beta$  and  $S_c$  were calculated using the erosion  
228 rate and measured curvature to produce idealized ridgetop profiles. Random noise was then  
229 applied to the profile, the grid was shifted, and the ‘synthetic’ curvature was calculated from  
230 the fitted 2<sup>nd</sup>-order polynomial. This process was repeated with variations in  $D$  until the  
231 synthetic curvature matched the curvature measured from the topographic data. We  
232 performed 250 iterations of adding random noise to a profile centered on the hilltop, and 250  
233 iterations of random noise to a profile centered 0.5 m from the hilltop. These calculations  
234 resulted in 500 values for the sediment transport coefficient that account for (1) sampling a  
235 continuous hillslope with gridded data, (2) random noise from the DEM, and (3) a potential  
236 mismatch between the actual location of the hillcrest and the highest pixel along the 1D ridge  
237 in the DEM.

238

### 239 **3. Results**

240 We find that the ‘raw’ hilltop curvature (i.e., uncorrected for grid-scale effects) is  
241 strongly correlated with the approximate square root of erosion rate:  $C_{HT} \propto E^{0.48}$  (Figure 2).  
242 The ‘corrected’ hilltop curvature is also correlated with erosion rate although the exponent in  
243 the regression increases to 0.53 (Figure 3). In addition, the transport coefficient (calculated  
244 from the corrected hilltop curvatures) varies with erosion rate, whereby  $D \propto E^{0.47}$  (Figure 4).

245 The transport efficiency is not correlated with any of the climate parameters (Figure  
246 5) nor with the ‘effective energy and mass transfer’ variable (plot not shown), a parameter  
247 which incorporates both MAT and MAP to represent the influence of climate on soil  
248 processes [Rasmussen and Tabor, 2007].

249 **4. Discussion**

250 Our results indicate that, at the sites we examined, erosion rate appears to have a  
251 dominant control on the efficiency of sediment transport. The apparent role of erosion rate on  
252 the efficiency of hillslope sediment transport and the insignificance of climate is unexpected  
253 considering that others have found a climatic influence on the value of  $D$  [Hurst *et al.*, 2013;  
254 Richardson *et al.*, 2019]. In contrast to our results, Richardson *et al.* [2019] compiled erosion  
255 rate and transport coefficient data from studies which used a variety of techniques to estimate  
256 these values, and their data included sites in a range of lithologies as well as from regions  
257 with a greater range in precipitation. As a result, their larger data set may be better suited for  
258 detecting an underlying climatic influence.

259 To explore how transport efficiency might increase with erosion rate, the factors  
260 contributing to soil creep can be assessed with two approaches. For discrete, intermittent  
261 large-scale soil creep events (e.g., tree throw), the transport efficiency can be calculated as

262  
263 
$$D = f_e \bar{V} \bar{d} \tag{7}$$

264  
265 where  $f_e$  is the frequency of events per unit area ( $T^{-1}L^{-2}$ ),  $\bar{V}$  is the average volume ( $L^3$ ) of soil  
266 displaced with each event, and  $\bar{d}$  is the average distance (L) that volume of soil is displaced  
267 [Gabet, 2000]. For example, in the case of tree throw, the transport coefficient will depend  
268 on the number of toppled trees over a period of time, the average volume of soil in the root  
269 plates, and the distance that the root plates are displaced [Gabet *et al.*, 2003]. We are not  
270 aware of any reason why any of these three factors would increase with erosion rate. Indeed,  
271 in the case of bioturbation,  $\bar{V}$  and  $f_e$  might be expected to *decrease*. For example, because

272 soils tend to be thinner where erosion rates are high [e.g., *Gabet et al.*, 2015], the volume of  
273 soil available for transport by three throw should decrease. In addition, the frequency of  
274 bioturbation might be expected to decrease in rapidly eroding landscapes because of lower  
275 plant biomass [*Milodowski et al.*, 2014].

276 For dilational creep processes in which soil particles are lofted up and then settle  
277 down due to gravity,  $D$  can be expressed as [*Furbish et al.*, 2009]

278

$$279 \quad D = kRhN_a \overline{\left(1 - \frac{P}{P_m}\right)^2} \cos^2 \theta \quad (8)$$

280

281 where  $k$  is an empirically determined dimensionless constant that accounts for particle shape  
282 and the relationship between mean free path length and the vertical displacement of particles,  
283  $R$  is particle radius (L),  $h$  is soil thickness (L),  $P$  is particle concentration ( $L^3L^{-3}$ ),  $P_m$  is the  
284 maximum value of  $P$ ,  $N_a$  is the particle activation rate ( $T^{-1}$ ),  $\theta$  is the hillslope angle ( $^\circ$ ) (equal  
285 to zero at the ridgecrest), and the overbar signifies vertically averaged quantities. The particle  
286 concentration (a function of soil bulk density) is not likely to be dependent on erosion rate to  
287 a significant degree and, if it is, the term in parentheses would likely decrease with increasing  
288 erosion rate, thereby suppressing the value of  $D$ . Because soils are thinner in rapidly eroding  
289 landscapes [e.g., *Gabet et al.*, 2015], variations in soil thickness also cannot account for the  
290 increase in transport efficiency with erosion rate; indeed, the inverse relationship between  
291 soil thickness and erosion rate should lead to an inverse relationship between  $D$  and  $E$ , the  
292 opposite of what we have found. With respect to particle activation rate, we are not aware of  
293 any studies that have correlated this variable with erosion rate; however, because rapidly

294 eroding hillslopes tend to have thinner and more exposed soils [e.g., *Gabet et al.*, 2015], the  
295 particle activation rate in these landscapes could potentially be higher, which could lead to an  
296 increase in  $D$  with  $E$ . For example, a decrease in vegetation biomass with increasing erosion  
297 rate [*Milodowski et al.*, 2014] could leave the soil surface more vulnerable to raindrop impact  
298 [*Dunne et al.*, 2010]. Nevertheless, as noted above, a reduction in biomass might also be  
299 expected to damp bioturbation, thereby reducing the transport efficiency.

300         The final variable from Eqn. (8) to be explored is particle diameter,  $R$ . Previous  
301 studies have documented an increase in particle diameter with erosion rate [*Attal et al.*, 2015;  
302 *Riebe et al.*, 2015]. Where erosion is slow, particles are exposed to weathering processes for  
303 longer periods of time because of longer soil residence times and, as a result, particles  
304 become smaller [e.g., *Mudd and Yoo*, 2010]. In Eqn. (8), particle size is a factor in the  
305 transport coefficient because it controls the mean free path of particles in a soil creeping by  
306 dilational processes [*Furbish et al.*, 2009]. Although field data from Neeley et al. [2019]  
307 suggest that coarser soils have a higher transport coefficient, laboratory experiments have  
308 demonstrated that, for the same input of energy, coarse-grained soils will creep faster than  
309 fine-grained soils [Supplement to *Deshpande et al.*, 2020]. In addition, of the various factors  
310 that could affect the rate of soil creep, particle size is the one with the most potential to vary  
311 by multiple orders-of-magnitude between watersheds eroding at different rates [*Marshall and*  
312 *Sklar*, 2012]. For example, while the data are limited, particle radius along a ridgeline  
313 increases with erosion rate at the Feather River site (Figure 6).

314         While particle size is a potential candidate for explaining the relationship between  
315 transport efficiency and erosion rate found here, this hypothesis raises some perplexing  
316 issues. First, whereas the relationship between particle size and erosion rate is likely to be

317 constant within a single region, one would expect them to vary between regions according to  
318 climate and lithology (although we tried to control for rock strength, variations in texture, for  
319 example, could affect particle size). However, despite the expected regional variations in  
320 these factors, the sites fall along the same  $D$  vs.  $E$  trendline (Figure 3). Second, because the  
321 more rapid weathering rates in wetter climates should lead to smaller soil particles [Marshall  
322 and Sklar, 2012], the transport coefficient should decrease in wetter climates. However, we  
323 find no relationship between mean annual precipitation and  $D$  (Figure 5).

324 Another potential explanation may be that the transport efficiency is sensitive to slope.  
325 Landscapes that are eroding quickly are generally steeper than those that are eroding more  
326 slowly. For example, the slopes at the ridgecrests ( $S_{HT}$ ) at our sites increase with the  
327 approximate square root of erosion rate (Figure 7). Some property of the soil (e.g., its  
328 resistance to disturbance) may be affected by the gradient such that its transport efficiency  
329 increases on steeper slopes (P. Richardson, pers. comm.). Furbish and Haff [2010] suggest  
330 that the rate at which soil is mobilized might also increase with slope. To explore the  
331 consequences of a slope-dependent transport coefficient, we define a new variable,  $D_s$  ( $L^2/T$ )

$$332 \quad D_s = KS \quad (10)$$

333 such that

$$334 \quad q_s = D_s S \quad (11a)$$

335 or

$$336 \quad q_s = KS^2 \quad (11b)$$

337 where  $K$  ( $L^2/T$ ) is a constant with the same properties as  $D$ . Inserting Eqn. (11b) into a  
338 statement of mass conservation

339 
$$\rho_r \frac{dz}{dt} = -\rho_s \frac{dq_s}{dx} \quad (12)$$

340 and integrating twice assuming steady state ( $dz/dt = E$ ) and  $\rho_r/\rho_s = 2$  yields

341 
$$E = KCS/2 \quad (13a).$$

342 To specify that this relationship is applied to the hilltops, we rewrite it as

343 
$$E = KC_{HT}S_{HT}/2 \quad (13b).$$

344 Thus, the assumption that the transport coefficient increases linearly with slope implies a  
345 linear relationship between the erosion rate and the product of curvature and slope. Indeed, a  
346 power-law regression between the two yields an exponent of unity, offering support for the  
347 hypothesis that the transport coefficient is slope-dependent (Figure 8). However, because  
348 slope and curvature are linearly related along a parabolic curve, Eqn. (13b) is functionally  
349 equivalent to  $E \propto C^2$  or  $C \propto E^{1/2}$ , which is the original relationship presented in Figure 3. In  
350 other words, the linear relationship between  $E$  and  $C_{HT}S_{HT}$  may simply be a mathematical  
351 artefact, and the sediment flux relationship represented by Eqn. (11b) would need to be  
352 validated independently. Finally, note that Eqn. (11b) is quite different from the nonlinear  
353 sediment flux equation proposed elsewhere [Andrews and Bucknam, 1987; Gabet, 2003;  
354 Roering *et al.*, 1999], particularly at lower slopes (Figure 9).

355 The lack of a clear and robust mechanistic link between  $D$  and  $E$ , as well as the square  
356 root dependency of the hilltop curvature on erosion rate when Eqn. (2) predicts a linear  
357 relationship, suggests that the present theory explaining the profile of soil-mantled hillslopes  
358 is incomplete. We tentatively propose that, in resistant lithologies, hillslope curvature may be  
359 partially, if not mostly, controlled by processes occurring within the bedrock, rather than the  
360 soil. Indeed, in an eroding landscape, the soil on a hill is just a thin mantle covering a much  
361 larger bedrock mass; the shape of the hill, therefore, should reflect the shape of the

362 underlying bedrock and the processes acting within it [e.g., *Rempe and Dietrich*, 2014].  
363 However, the absence of any climatic influence in our results suggests that these bedrock  
364 processes are not associated with the typical chemical and physical weathering processes;  
365 instead, they are likely related to a more universal mechanism. Recent work has begun  
366 investigating how, even in soil-mantled landscapes, the generation of fractures in bedrock by  
367 topographic stresses may exert an important influence on landform shape [e.g., *Clair et al.*,  
368 2015; *Pelletier*, 2017; *Slim et al.*, 2015]. However, whereas the regional tectonic stress is an  
369 important contributor to topographic stresses [e.g., *Clair et al.*, 2015; *Miller and Dunne*,  
370 1996], the tectonic stress regime varies widely between our sites. For example, the regional  
371 stresses are compressional in the San Gabriel Mountains but extensional in the Wasatch  
372 Mountains and the Feather River study area [*Heidbach et al.*, 2016; *Wakabayashi and*  
373 *Sawyer*, 2000]. Therefore, the alignment of these sites along the same trendline (Figure 2)  
374 suggests that our present understanding of rock fracture by topographic stresses is unable to  
375 explain our results.

376         One potential avenue for further investigations may be an examination of the time-  
377 dependent nature of fracture growth. At high erosion rates, near-surface bedrock is  
378 rejuvenated more quickly, thereby limiting the fracture density. In contrast, in environments  
379 where the erosion rate is slower and the rejuvenation of the surface occurs less frequently, the  
380 near-surface bedrock may have a higher fracture density as it accumulates damage over time.  
381 The relationship found here between hilltop curvature and erosion rate, therefore, may be  
382 related to the strength of the underlying rock mass in a way that is not yet understood. As a  
383 preliminary test of this idea, we analyzed the data from four sites that met our criteria but  
384 were underlain by presumably weak lithologies, sedimentary bedrock or highly sheared

385 metamorphic bedrock [*Perron et al.*, 2012; *Richardson et al.*, 2019]. A comparison of the  
386 hilltop curvatures between our original data-set consisting of resistant rocks and the data  
387 from the weaker lithologies suggests that, for the same erosion rate, the weaker bedrock  
388 forms hilltops with lower curvatures (Figure 10). While the data set from presumably weak  
389 lithologies is limited, it supports our hypothesis that weaker bedrock is associated with lower  
390 curvatures. Although one might argue that the lower curvatures seen in hillslopes underlain  
391 by weaker lithologies could be a result of higher transport efficiencies, a clear mechanistic  
392 link between bedrock strength and transport efficiency is lacking (see below), especially  
393 considering that most soil creep processes (e.g., tree throw) do not appear to be limited by  
394 soil texture.

395         If bedrock processes have an important influence on hillslope form, then hilltop  
396 curvature cannot be used for estimating the transport coefficient, at least in landscapes  
397 underlain by resistant rock. This limitation might explain why we were unable to detect any  
398 climatic influence on  $D$ , in contrast to compilations that include estimates of  $D$  from a variety  
399 of techniques [*Hurst et al.*, 2013; *Richardson et al.*, 2019]. In addition, if hillslope form is  
400 primarily dependent on the underlying bedrock, estimates of  $D$  based on topographic  
401 characteristics might be expected to be of different magnitudes than estimates from other  
402 techniques. Indeed, in the compilation presented by Richardson et al. [2019], transport  
403 coefficients estimated from relief and hilltop curvature are generally 5 – 10 times higher than  
404 those estimated from the modeling of scarps for the same aridity index (a factor that was  
405 determined to be a control on  $D$ ) despite the fact that estimates based on scarp evolution were  
406 often performed on slopes comprised of unconsolidated sediment, which might be expected  
407 to have higher values of  $D$ . Therefore, the mismatch between the estimates of the transport

408 coefficient based on topographic metrics and those based on other techniques suggests that  
409 some other factor is influencing hillslope shape.

## 410 **5. Conclusions**

411 The square-root dependency of hilltop curvature on erosion rate challenges the  
412 prevailing theory linking soil creep to the shape of soil-mantled hillslopes, which predicts a  
413 linear relationship between the two. This dependency could be explained if the transport  
414 coefficient also varies with the square root of erosion rate. However, we are unable to  
415 propose a robust mechanism linking the transport coefficient to the erosion rate. Given the  
416 difficulties in accounting for our results within the standard theory of hillslope evolution, we  
417 tentatively propose that in landscapes underlain by resistant lithologies, hillslope curvature is  
418 not related to soil creep but is, instead, controlled by processes in the underlying bedrock.

419 Finally, the robust relationship between ridgetop curvature and erosion rate across a  
420 range of climatic conditions suggests that the latter can be estimated directly from  
421 topographic analysis in rock types similar to those analyzed in this study. However, erosion  
422 rates determined with this procedure must incorporate uncertainties in the original  $^{10}\text{Be}$   
423 erosion rate measurements, uncertainties in the curvature measurements, and the uncertainty  
424 in the regression between  $C_{\text{HT}}$  and  $E$ . Nevertheless, our results have the potential for  
425 providing a simple approach for estimating watershed-scale erosion rates through the  
426 measurement of hilltop curvatures.

427

## 428 **Acknowledgments**

429 Idaho field work for this project was conducted with assistance from B. Wood, S.  
430 Powell, and E. Hewitt. There were no real or perceived financial conflicts of interest for any

431 author nor did any author have an affiliation that could be perceived as having a conflict of  
432 interest with respect to the results of this paper. The data supporting the conclusions can be  
433 found in the tables and references. This project was partially funded by graduate student  
434 research grants from GSA and SJSU. LiDAR elevation data were acquired with a Seed  
435 Project from the National Center for Airborne Laser Mapping in the summer of 2011.  
436 Software used for analysis was developed under NERC grant NE/J009970/1. We are grateful  
437 to J. Pelletier, J. Roering, and P. Richardson for their careful reviews and helpful comments,  
438 and D. Furbish for extended and insightful discussions.

439

#### 440 **Data Availability Statement**

441 Original data for this research are provided in Tables 1 and 2. Additional data were  
442 compiled from Belmont et al. [2007], Binnie et al. [2007], Dibiase et al. [2010], Duxbury  
443 [2009], Hurst et al. [2012], Richardson et al. [2019], and Riebe et al. [2001].

#### 444 **References**

- 445 Anderson, H. W., G. B. Coleman, and P. J. Zinke (1959), Summer slides and winter scour,  
446 dry-wet erosion in Southern California mountains: U.S.D.A., Forest Service, *Pacific*  
447 *Southwest Forest and Range Experiment Station Technical Paper PSW-36*.
- 448 Anderson, R. S., S. P. Anderson, and G. E. Tucker (2013), Rock damage and regolith  
449 transport by frost: An example of climate modulation of the geomorphology of the  
450 critical zone, *Earth Surface Processes and Landforms*, 38(3), 299-316.
- 451 Andrews, D. J., and R. C. Bucknam (1987), Fitting degradation of shoreline scarps by a  
452 nonlinear diffusion model, *Journal of Geophysical Research*, 92(B12), 12,857-  
453 812,867.
- 454 Attal, M., S. M. Mudd, M. D. Hurst, B. Weinman, K. Yoo, and M. Naylor (2015), Impact of  
455 change in erosion rate and landscape steepness on hillslope and fluvial sediments  
456 grain size in the Feather River Basin (Sierra Nevada, California), *Earth Surface*  
457 *Dynamics*, 2, 1047-1092.
- 458 Belmont, P., F. J. Pazzaglia, and J. C. Gosse (2007), Cosmogenic  $^{10}\text{Be}$  as a tracer for  
459 hillslope and channel sediment dynamics in the Clearwater River, western  
460 Washington State, *Earth and Planetary Science Letters*, 264, 123-135.

- 461 Ben-Asher, M., I. Haviv, J. J. Roering, and O. Crouvi (2017), The influence of climate and  
462 microclimate (aspect) on soil creep efficiency: Cinder cone morphology and  
463 evolution along the eastern Mediterranean Golan Heights, *Earth Surface Processes  
464 and Landforms*, 42(15), 2649-2662.
- 465 Binnie, S. A., W. M. Phillips, M. A. Summerfield, and K. Fifield (2007), Tectonic uplift,  
466 threshold hillslopes, and denudation rates in a developing mountain range, *Geology*,  
467 35, 743-746.
- 468 Binnie, S. A., T. J. Dunai, E. Voronina, T. Goral, S. Heinze, and A. Dewald (2015),  
469 Separation of Be and Al for AMS using single-step column chromatography, *Nuclear  
470 Instruments and Methods in Physics Research Section B: Beam Interactions with  
471 Materials and Atoms*, 361, 397-401.
- 472 Brown, E. T., R. F. Stallard, M. C. Larsen, G. M. Raisbeck, and F. Yiou (1995), Denudation  
473 rates determined from the accumulation of in situ-produced <sup>10</sup>Be in the Luquillo  
474 Experimental Forest, Puerto Rico, *Earth and Planetary Science Letters*, 129(1-4),  
475 193-202.
- 476 Carson, M. A., and M. J. Kirkby (1972), *Hillslope form and process*, 475 pp., Cambridge  
477 University Press, New York.
- 478 Clair, J. S., S. Moon, W. S. Holbrook, J. T. Perron, C. S. Riebe, S. J. Martel, B. Carr, C.  
479 Harman, K. Singha, and D. d. Richter (2015), Geophysical imaging reveals  
480 topographic stress control of bedrock weathering, *Science*, 350, 534-538.
- 481 Culling, W. E. H. (1963), Soil creep and the development of hillside slopes, *Journal of  
482 Geology*, 71, 127-161.
- 483 Denny, C., and J. Goodlett (1956), Microrelief resulting from fallen trees, *USGS Professional  
484 Publication*, 288, 59-68.
- 485 Deshpande, N., D. J. Furbish, P. Arratia, and D. Jerolmack (2020), The perpetual fragility of  
486 creeping hillslopes, *EarthArXiv*, doi:10.31223/osf.io/qc9jh.
- 487 Dewald, A., et al. (2013), CologneAMS, a dedicated center for accelerator mass spectrometry  
488 in Germany, *Nuclear Instruments and Methods in Physics Research Section B: Beam  
489 Interactions with Materials and Atoms*, 294, 18-23.
- 490 DiBiase, R. A., K. X. Whipple, A. M. Heimsath, and W. B. Ouimet (2010), Landscape form  
491 and millennial erosion rates in the San Gabriel Mountains, CA, *Earth and Planetary  
492 Science Letters*, 289, 134-144.
- 493 Dunne, T., D. V. Malmon, and S. M. Mudd (2010), A rain splash transport equation  
494 assimilating field and laboratory measurements, *Journal of Geophysical Research -  
495 Earth Surface*, 115(F01001), 1-16.
- 496 Duxbury, J. (2009), Erosion rates in and around the Shenandoah National Park, VA,  
497 determined using analysis of cosmogenic <sup>10</sup>Be, MS thesis, 123 pp, University of  
498 Vermont.
- 499 Fernandes, N. F., and W. E. Dietrich (1997), Hillslope evolution by diffusive processes: the  
500 timescale for equilibrium adjustments, *Water Resources Research*, 33(6), 1307-1318.
- 501 Furbish, D. J., and P. K. Haff (2010), From divots to swales: Hillslope sediment transport  
502 across divers length scales, *Journal of Geophysical Research*, 115(F03001),  
503 doi:10.1029/2009JF001576.
- 504 Furbish, D. J., P. K. Haff, W. E. Dietrich, and A. M. Heimsath (2009), Statistical description  
505 of slope-dependent soil transport and the diffusion-like coefficient, *Journal of  
506 Geophysical Research*, 114(F00A05), doi:10.1029/2009JF001267.

507 Gabet, E. J. (2000), Gopher bioturbation: Field evidence for nonlinear hillslope diffusion,  
508 *Earth Surface Processes and Landforms*, 25(13), 1419-1428.

509 Gabet, E. J. (2003), Sediment transport by dry ravel, *Journal of Geophysical Research*,  
510 108(B1), 2050, 2010.1029/2001JB001686.

511 Gabet, E. J. (2020), Lithological and structural controls on river profiles and networks in the  
512 northern Sierra Nevada, *Geological Society of America Bulletin*, 132(3-4), 655-667.

513 Gabet, E. J., O. J. Reichman, and E. Seabloom (2003), The effects of bioturbation on soil  
514 processes and sediment transport, *Annual Review of Earth and Planetary Sciences*,  
515 31, 259-273.

516 Gabet, E. J., S. M. Mudd, D. T. Milodowski, K. Yoo, M. D. Hurst, and A. Dosseto (2015),  
517 Local topography and erosion rate control regolith thickness along a ridgeline in the  
518 Sierra Nevada, California, *Earth Surface Processes and Landforms*, 40(13), 1779-  
519 1790.

520 Gilbert, G. K. (1909), The convexity of hillslopes, *Journal of Geology*, 17, 344-350.

521 Granger, D. E., J. W. Kirchner, and R. C. Finkel (1996), Spatially averaged long-term  
522 erosion rates measured from in situ-produced cosmogenic nuclides in alluvial  
523 sediment, *Journal of Geology*, 104(3), 249-257.

524 Grieve, S. W. D., S. M. Mudd, and M. D. Hurst (2016), How long is a hillslope?, *Earth*  
525 *Surface Processes and Landforms*, 41(8), 1039-1054.

526 Hack, J. T. (1973), Stream-profile analysis and stream-gradient index, *Journal of Research of*  
527 *the U.S. Geological Survey*, 1(4), 421-429.

528 Hanks, T. C. (2000), The age of scarplike landforms from diffusion - equation analysis,  
529 *Quaternary Geochronology: Methods and Applications*, 313-338.

530 Hanks, T. C., and D. P. Schwartz (1987), Morphologic dating of the pre-1983 fault scarp on  
531 the Lost River Fault at Doublespring Pass Road, Custer County, Idaho, *Bulletin of the*  
532 *Seismological Society of America*, 77, 837-846.

533 Harel, M. A., S. M. Mudd, and M. Attal (2016), Global analysis of the stream power law  
534 parameters based on worldwide <sup>10</sup>Be denudation rates, *Geomorphology*, 268, 184-  
535 196.

536 Heidbach, O., M. Rajabi, K. Reiter, M. Ziegler, and W. Team (2016), World Stress Map  
537 Database Release 2016. V. 1.1, edited, GFZ Data Services.

538 Heimsath, A. M., D. J. Furbish, and W. E. Dietrich (2005), The illusion of diffusion: Field  
539 evidence for depth-dependent sediment transport, *Geology*, 33(12), 949-952.

540 Hurst, M. D., S. M. Mudd, R. C. Walcott, M. Attal, and K. Yoo (2012), Using hilltop  
541 curvature to derive the spatial distribution of erosion rates, *Journal of Geophysical*  
542 *Research - Earth Surface*, 115, 1-19.

543 Hurst, M. D., S. M. Mudd, K. Yoo, M. Attal, and R. C. Walcott (2013), Influence of  
544 lithology on hillslope morphology and response to tectonic forcing in the northern  
545 Sierra Nevada of California, *Journal of Geophysical Research - Earth Surface*, 118,  
546 832-851.

547 Kirchner, P. B., R. C. Bales, N. P. Molotoch, J. Flanagan, and Q. Guo (2014), LiDAR  
548 measurement of seasonal snow accumulation along an elevation gradient in the  
549 southern Sierra Nevada, California, *Hydrological Earth Systems Science*, 18, 4261-  
550 4275.

551 Kohl, C. P., and K. Nishiizumi (1992), Chemical isolation of quartz for measurement of in-  
552 situ -produced cosmogenic nuclides, *Geochimica et Cosmochimica Acta*, 56(9), 3583-  
553 3587.

554 Marshall, J. A., and L. S. Sklar (2012), Mining soil databases for landscape-scale patterns in  
555 the abundance and size distribution of hillslope rock fragments, *Earth Surface  
556 Processes and Landforms*, 37(3), 287-300.

557 Mifsud, C., T. Fujioka, and D. Fink (2013), Extraction and purification of quartz in rock  
558 using hot phosphoric acid for in situ cosmogenic exposure dating, *Nuclear  
559 Instruments and Methods in Physics Research Section B: Beam Interactions with  
560 Materials and Atoms*, 294, 203-207.

561 Miller, D. J., and T. Dunne (1996), Topographic perturbations of regional stresses and  
562 consequent bedrock fracturing, *Journal of Geophysical Research*, 101B, 25,523-  
563 525,536.

564 Milodowski, D. T., S. M. Mudd, and E. T. Mitchard (2014), Erosion rates as a potential  
565 bottom-up control of forest structural characteristics in the Sierra Nevada Mountains,  
566 *Ecology*, 96(1), 31-38.

567 Milodowski, D. T., S. M. Mudd, and E. T. A. Mitchard (2015), Topographic roughness as a  
568 signature of the emergence of bedrock in eroding landscapes, *Earth Surf. Dynam.*,  
569 3(4), 483-499.

570 Mudd, S. M. (2017), Detection of transience in eroding landscapes, *Earth Surface Processes  
571 and Landforms*, 42(1), 24-41.

572 Mudd, S. M., and K. Yoo (2010), Reservoir theory for studying the geochemical evolution of  
573 soils, *Journal of Geophysical Research: Earth Surface*, 115(F03030).

574 Mudd, S. M., M. Harel, M. D. Hurst, S. W. D. Grieve, and S. M. Marrero (2016), The  
575 CAIRN method: Automated, reproducible calculation of catchment-averaged  
576 denudation rates from cosmogenic radionuclide concentrations, *Earth Surface  
577 Dynamics*, 4, 655-674.

578 Neely, A. B., R. A. DiBiase, L. B. Corbett, P. R. Bierman, and M. W. Caffee (2019),  
579 Bedrock fracture density controls on hillslope erodibility in steep, rocky landscapes  
580 with patchy soil cover, southern California, USA, *Earth and Planetary Science  
581 Letters*, 522, 186-197.

582 Nishiizumi, K., M. Imamura, M. W. Caffee, J. R. Southon, R. C. Finkel, and J. McAninch  
583 (2007), Absolute calibration of <sup>10</sup>Be AMS standards, *Nuclear Instruments and  
584 Methods in Physics Research Section B: Beam Interactions with Materials and  
585 Atoms*, 258(2), 403-413.

586 NOAA (2016), National Center for Environmental Information, edited.

587 Pelletier, J. D. (2017), Quantifying the controls on potential soil production rates: a case  
588 study of the San Gabriel Mountains, California, *Earth Surf. Dynam.*, 5(3), 479-492.

589 Pelletier, J. D., et al. (2011), Calibration and testing of upland hillslope evolution models in a  
590 dated landscape: Banco Bonito, New Mexico, *Journal of Geophysical Research:  
591 Earth Surface*, 116(F4).

592 Perron, J. T., P. W. Richardson, K. L. Ferrier, and M. Lapotre (2012), The root of branching  
593 river networks, *Nature*, 492, 100-103.

594 PRISM (2014), PRISM Climate Group, edited.

595 Rasmussen, C., and N. Tabor (2007), Applying a quantitative pedogenic energy model across  
596 a range of environmental gradients, *Soil Science Society of America Journal*, 71(6),  
597 1719-1729.

598 Rempe, D. M., and W. E. Dietrich (2014), A bottom-up control on fresh-bedrock topography  
599 under landscapes, *Proceedings of the National Academy of Sciences*, 111(18), 6576-  
600 6581.

601 Richardson, P. W., J. T. Perron, and N. D. Schurr (2019), Influences of climate and life on  
602 hillslope sediment transport, *Geology*, 47, 423-426.

603 Riebe, C. S., J. W. Kirchner, D. E. Granger, and R. C. Finkel (2001), Minimal climatic  
604 control on erosion rates in the Sierra Nevada, California, *Geology*, 29(5), 447-450.

605 Riebe, C. S., L. S. Sklar, C. E. Lukens, and D. L. Shuster (2015), Climate and topography  
606 control the size and flux of sediment produced on steep mountain slopes, *Proceedings*  
607 *of the National Academy of Sciences*, 112(51), 15574-15579.

608 Roering, J. J., J. W. Kirchner, and W. E. Dietrich (1999), Evidence for non-linear, diffusive  
609 sediment transport on hillslopes and implications for landscape morphology, *Water*  
610 *Resources Research*, 35(3), 853-870.

611 Roering, J. J., J. W. Kirchner, and W. E. Dietrich (2001a), Hillslope evolution by nonlinear,  
612 slope-dependent transport: steady state morphology and equilibrium adjustment  
613 timescales, *Journal of Geophysical Research*, 106(B8), 16499-16513.

614 Roering, J. J., J. T. Perron, and J. W. Kirchner (2007), Functional relationships between  
615 denudation and hillslope form and relief, *Earth and Planetary Science Letters*,  
616 264(1), 245-258.

617 Roering, J. J., J. W. Kirchner, L. S. Sklar, and W. E. Dietrich (2001b), Hillslope evolution by  
618 nonlinear creep and landsliding: An experimental study, *Geology*, 29(2), 143-146.

619 Roering, J. J., J. Marshall, A. M. Booth, M. Mort, and Q. Jin (2010), Evidence for biotic  
620 controls on topography and soil production, *Earth and Planetary Science Letters*,  
621 298, 183-190.

622 Saucedo, G. J., and D. L. Wagner (1992), Geologic map of the Chico quadrangle, California,  
623 Division of Mines and Geology.

624 Slim, M., J. T. Perron, S. J. Martel, and K. Singha (2015), Topographic stress and rock  
625 fracture: a two-dimensional numerical model for arbitrary topography and  
626 preliminary comparison with borehole observations, *Earth Surface Processes and*  
627 *Landforms*, 40(4), 512-529.

628 Trabucco, A., and R. Zomer (2019), *Global Aridity Index and Potential Evapotranspiration*  
629 *(ET0) Climate Database v2. CGIAR Consortium for Spatial Information*  
630 *(CGIAR-CSI). Published online, available from the CGIAR-CSI GeoPortal at*  
631 *<https://cgiarcsi.community>.*

632 Wakabayashi, J., and T. L. Sawyer (2000), Neotectonics of the Sierra Nevada and the Sierra  
633 Nevada-Basin and Range transition, California, with field trip stop descriptions for  
634 the northeastern Sierra Nevada, in *Field Guide to the Geology and Tectonics of the*  
635 *Northern Sierra Nevada*, edited by E. R. Brooks and L. T. Dida, pp. 173 - 212,  
636 California Division of Mines and Geology.

637 Wood, R. (2013), Transient hillslope response to an incision wave sweeping up a watershed:  
638 a case study from the Salmon River, MS thesis, 42 pp, San Jose State University, San  
639 Jose, CA.

640

641

642

643 Figure captions

644 **Figure 1.** Map of the United States showing the locations of the study sites.

645

646 **Figure 2.** Median hilltop curvature increases with the approximate square root of erosion  
647 rate. Because ridgetops have negative curvature, the absolute value of curvature is plotted to  
648 allow a power-law regression. For clarity, error bars are not shown here; uncertainties are  
649 presented in Table 1.

650

651 **Figure 3.** Corrected median hilltop curvature vs. erosion rate. Accounting for grid-resolution  
652 effects modifies the relationship between curvature and erosion rate, albeit only slightly  
653 (compare with Figure 2).

654

655 **Figure 4.** Inferred transport efficiency ( $D$ ) increases approximately with the square root of  
656 erosion rate.  $D$  was calculated using the corrected hilltop curvatures.

657

658 **Figure 5.** Inferred transport efficiency ( $D$ ) vs. various climatic measures. Inferred transport  
659 efficiency does not depend significantly on mean annual precipitation (A), mean annual  
660 temperature (B), or the aridity index (C). Note that the plot for mean annual temperature does  
661 not include the data set from Richardson et al. [2019], which did not provide these values.

662

663 **Figure 6.** Geometric mean of particle size ( $R$ ) increases with inferred erosion rate ( $E$ ) at the  
664 Feather River site [Gabet et al., 2015]. Particle sizes of soil surface samples were measured  
665 at regular intervals along a ridge with a gradient in erosion rates. Because local topography

666 along the ridgeline (i.e., saddles and knobs) was found to have a strong control on soil  
667 properties at this site, we present here only the data from the knobs. Erosion rate calculated  
668 from ridgetop curvatures using the relationship reported in the present study.  $1\sigma$  for particle  
669 size data averages 5.8 mm (error bars not shown for clarity).

670

671 **Figure 7.** Mean slope at the ridgeline increases with erosion rate. The steeper slopes  
672 generally found in rapidly eroding landscapes can also be recognized along the ridgecrests.

673

674 **Figure 8.** Product of hilltop curvature and slope vs. erosion rate. The nearly linear  
675 relationship between the two supports a sediment flux law of the form  $q_s = KS^2$ . This linear  
676 relationship may be a mathematical artefact.

677

678 **Figure 9.** Comparison of nonlinear sediment flux equations. Dashed line represents the  
679 commonly used nonlinear equation calibrated with values determined in Roering et al.  
680 [1999]. Solid line represents fluxes calculated with Eqn. (11b) and calibrated to provide a  
681 comparison with the dashed line. Fluxes were calculated over the range of hilltop gradients  
682 measured at our field sites. Note that a linear regression (not shown) through the dashed line  
683 yields an  $R^2$  of 0.9999, confirming the use of Eqn. (1) as an appropriate substitute for the  
684 standard nonlinear equation at low slopes.

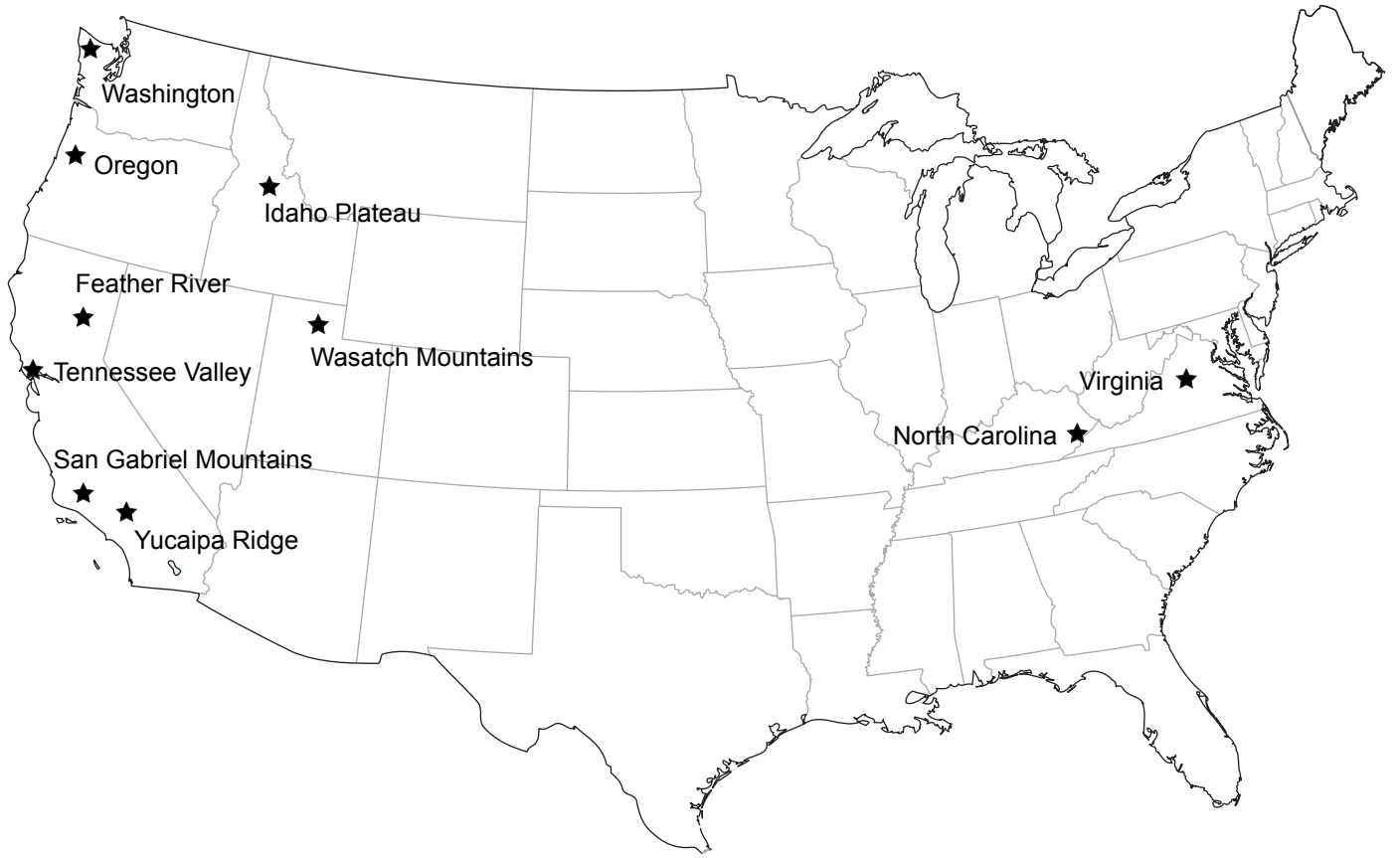
685

686 **Figure 10.** Curvature vs. erosion rate according to rock type. For the same erosion rate, the  
687 hilltop curvature is lower at sites underlain with presumably weaker bedrock when compared  
688 to sites with stronger bedrock. Sites shown with the square markers are Tennessee Valley

689 (CA), Oregon Coast Range (OR), Gabilan Mesa (CA), and Allegheny Plateau (PA) [*Perron*  
690 *et al.*, 2012; *Richardson et al.*, 2019].

691

Figure 1.



Washington

Oregon

Idaho Plateau

Feather River

Tennessee Valley

San Gabriel Mountains

Yucaipa Ridge

Wasatch Mountains

North Carolina

Virginia

Figure 2.

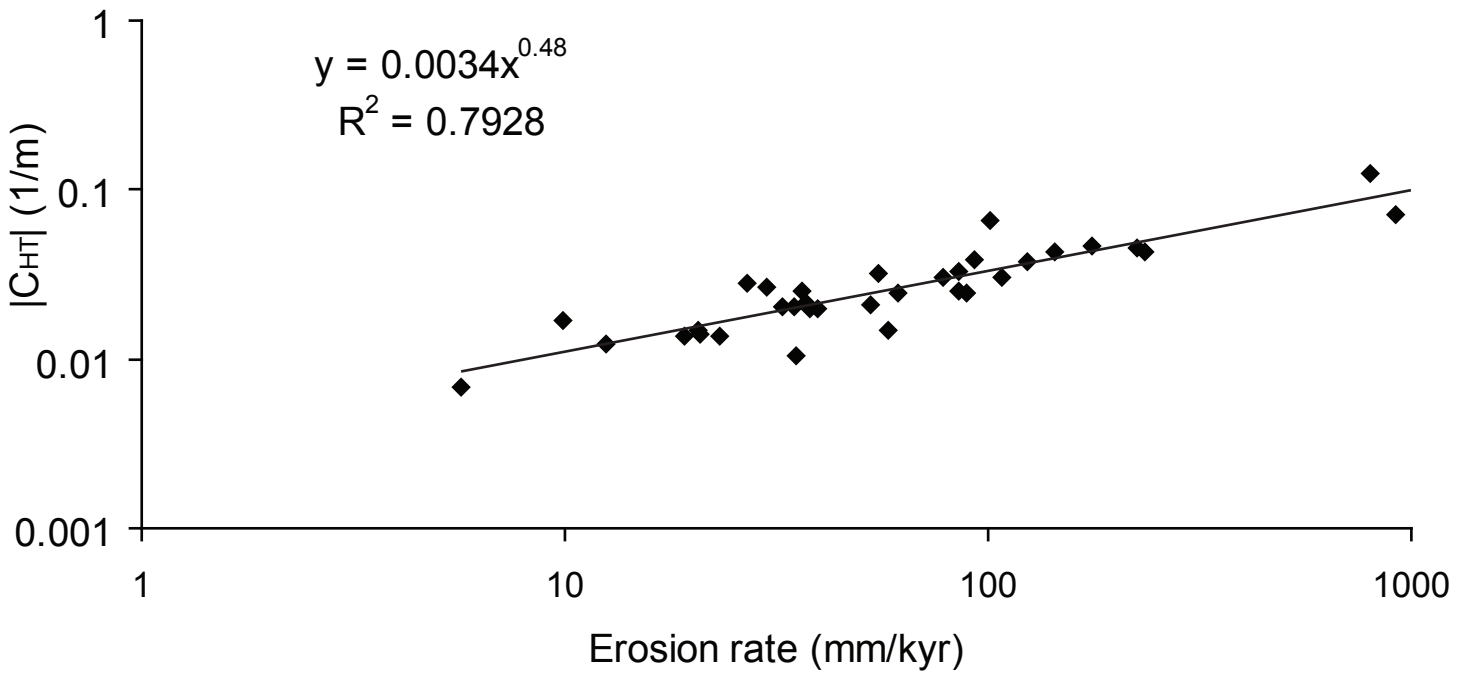
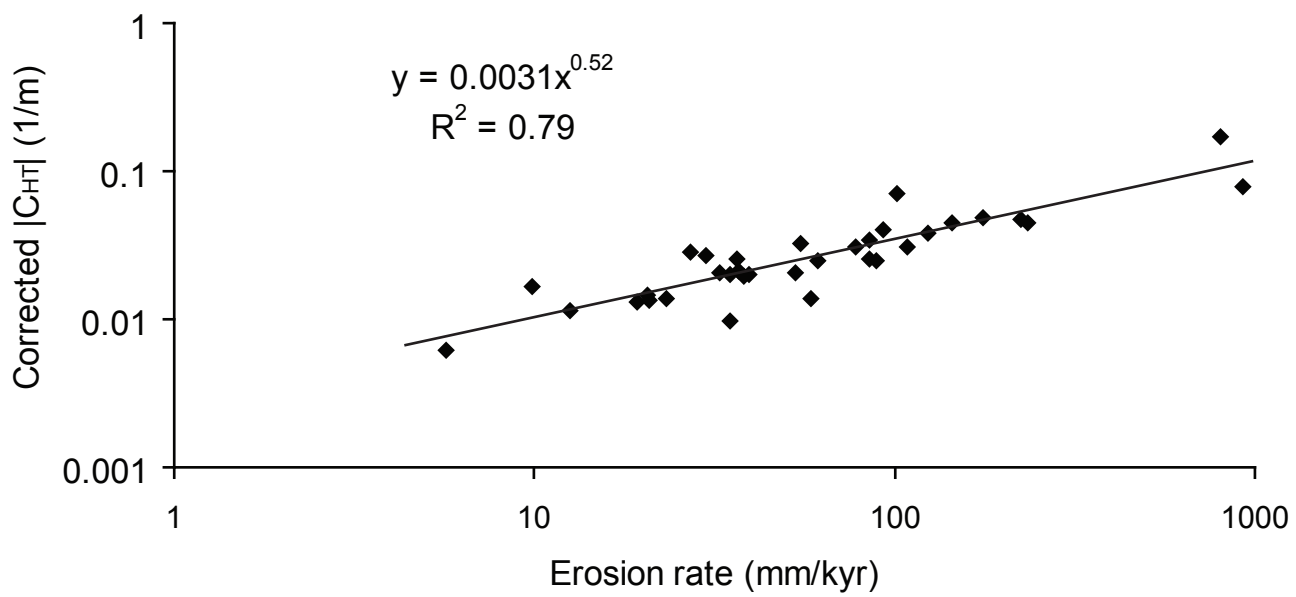


Figure 3.



**Figure 4.**

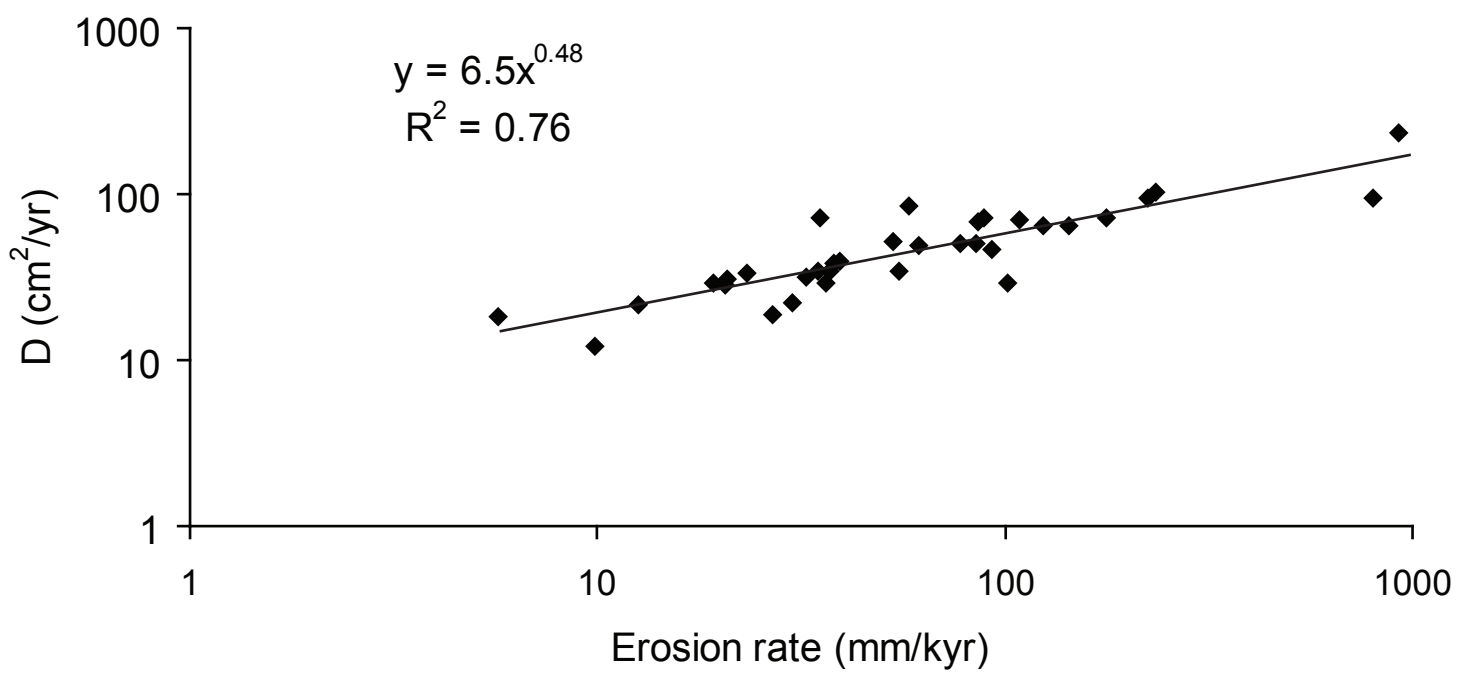
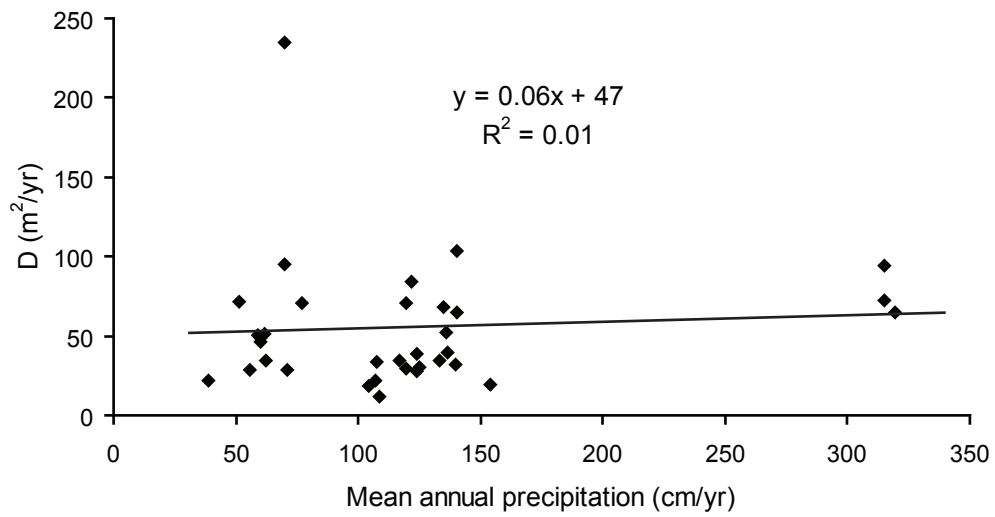
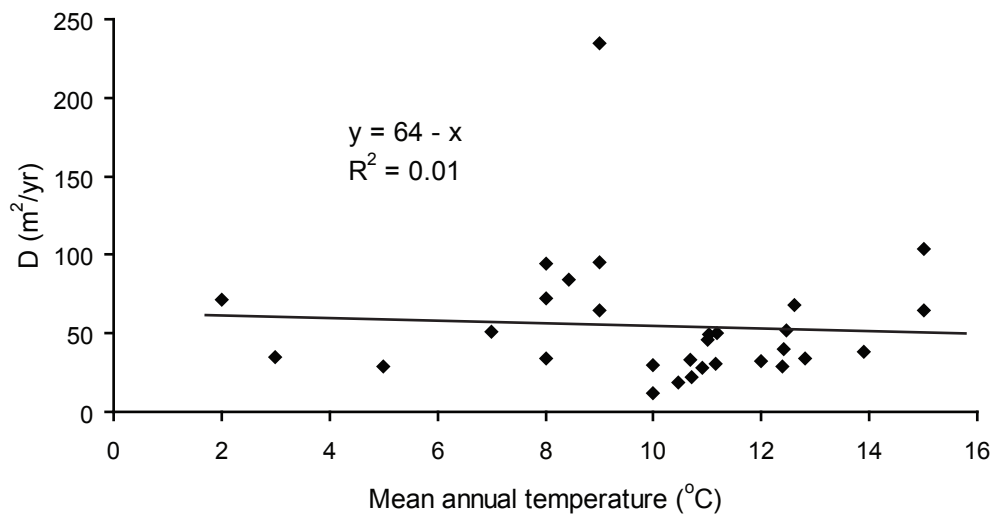


Figure 5.

(A)



(B)



(C)

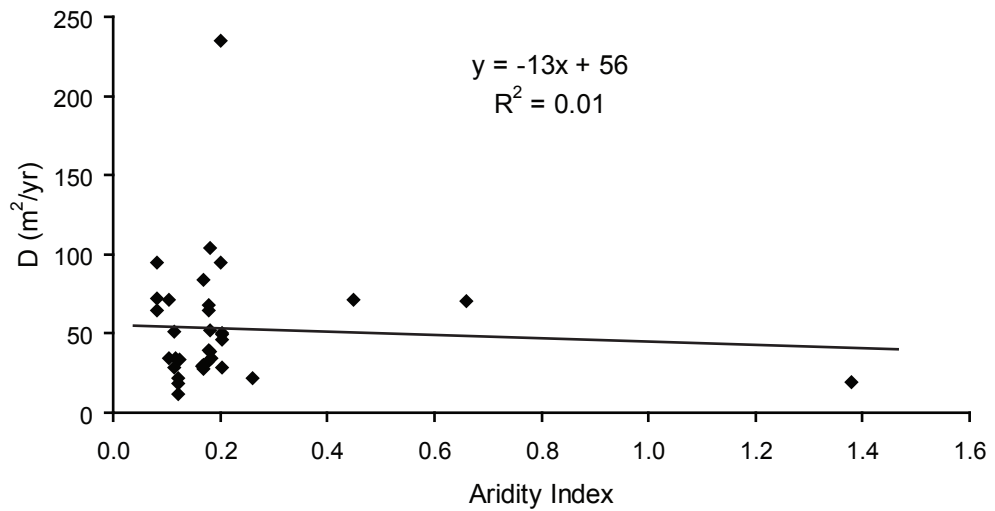


Figure 6.

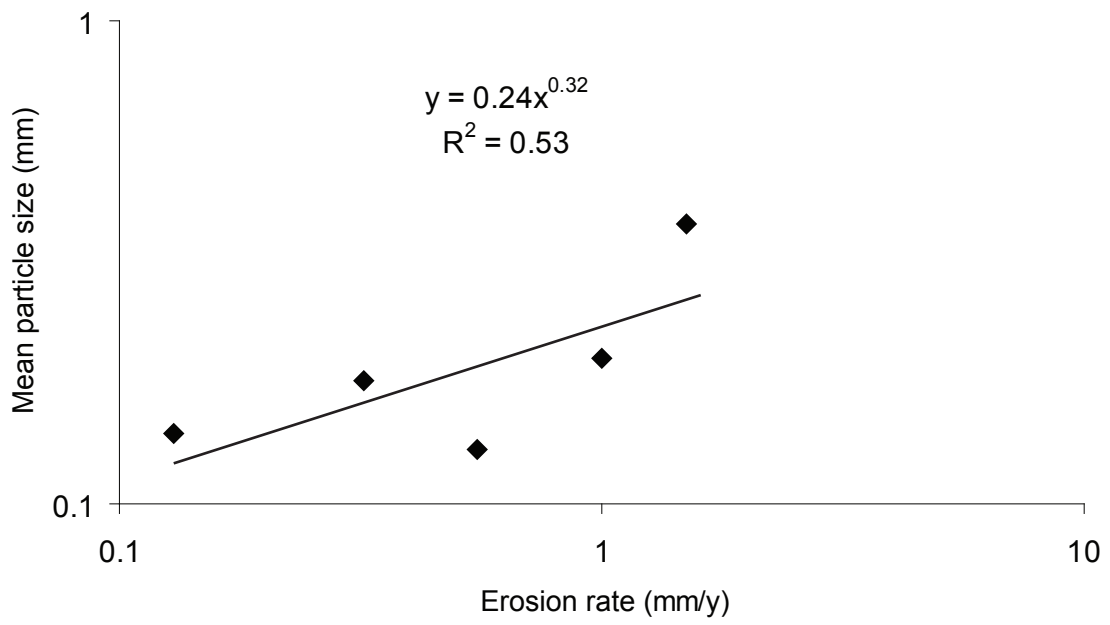


Figure 7.

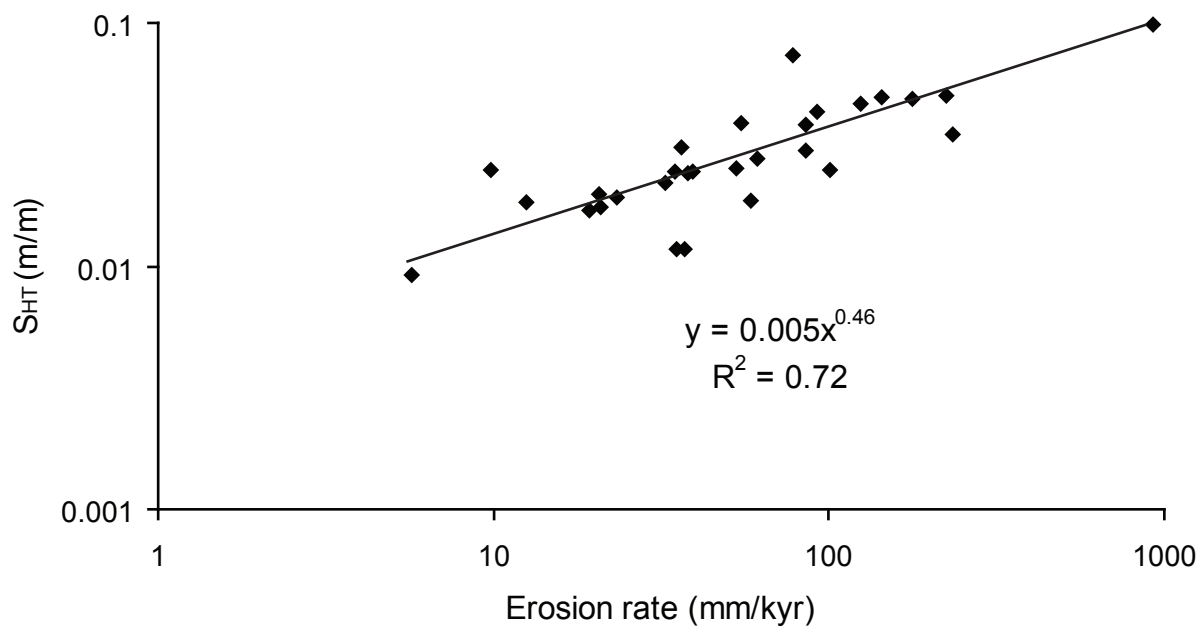


Figure 8.

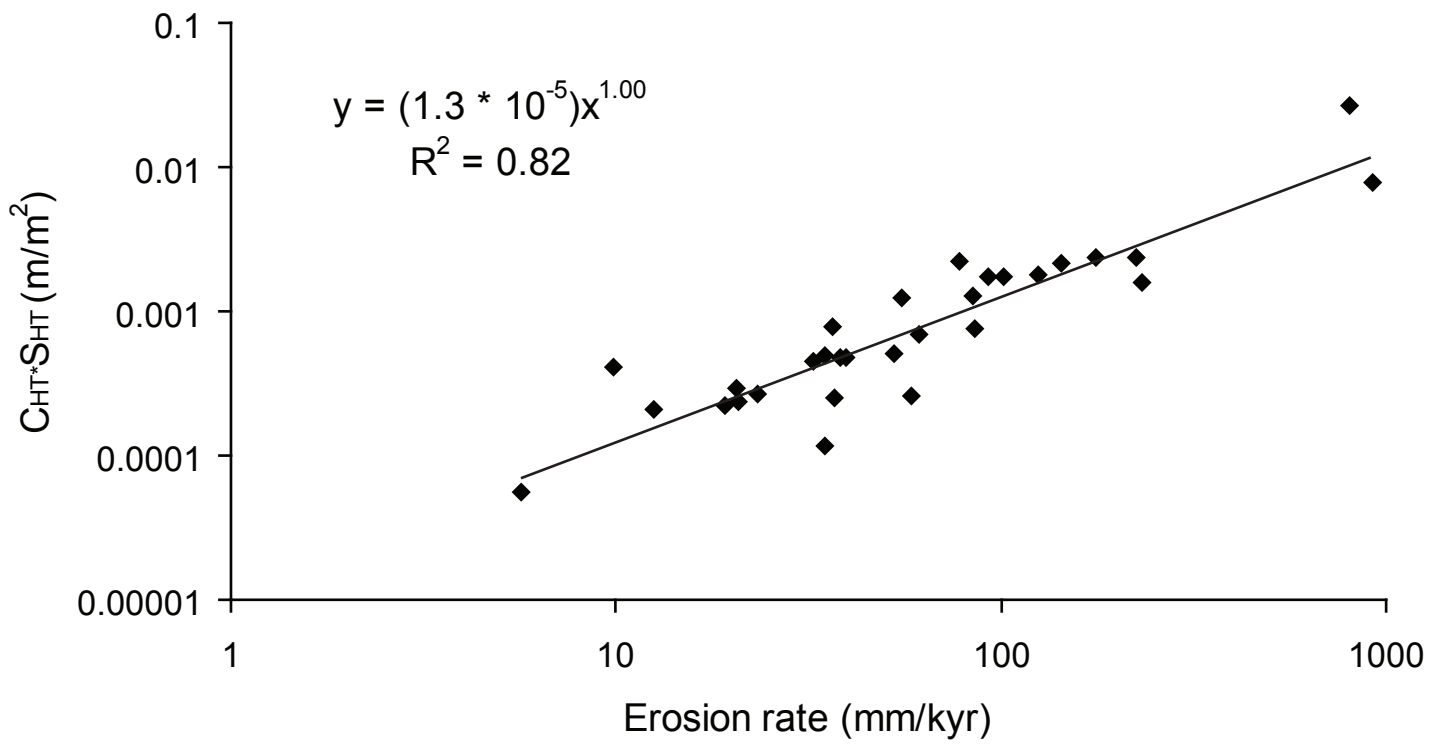


Figure 9.

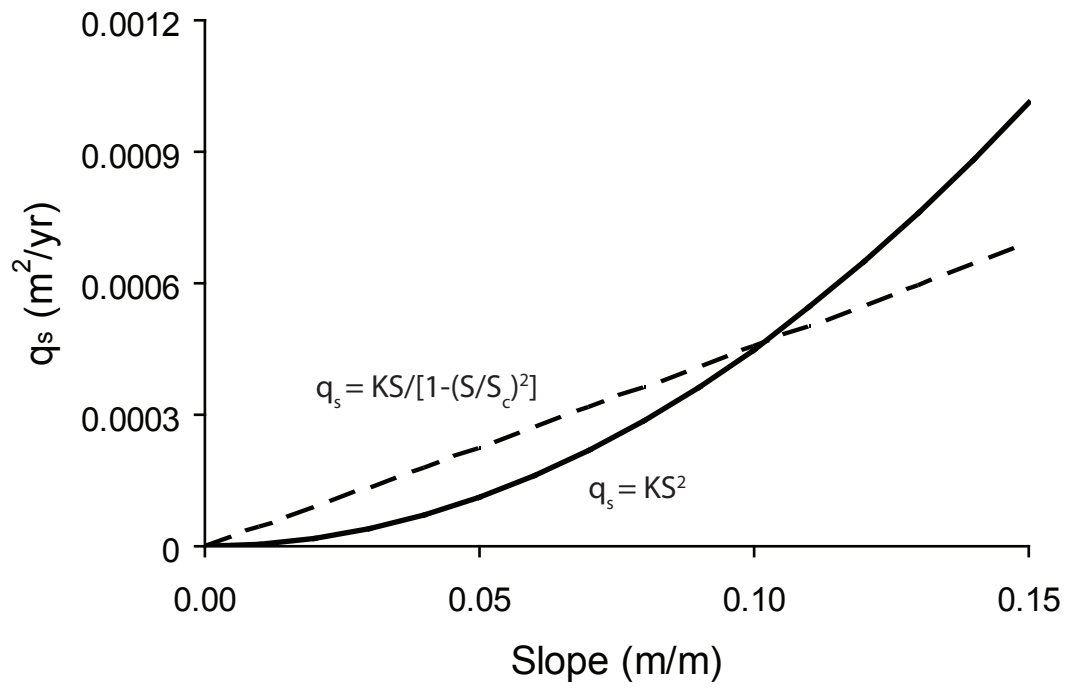


Figure 10.

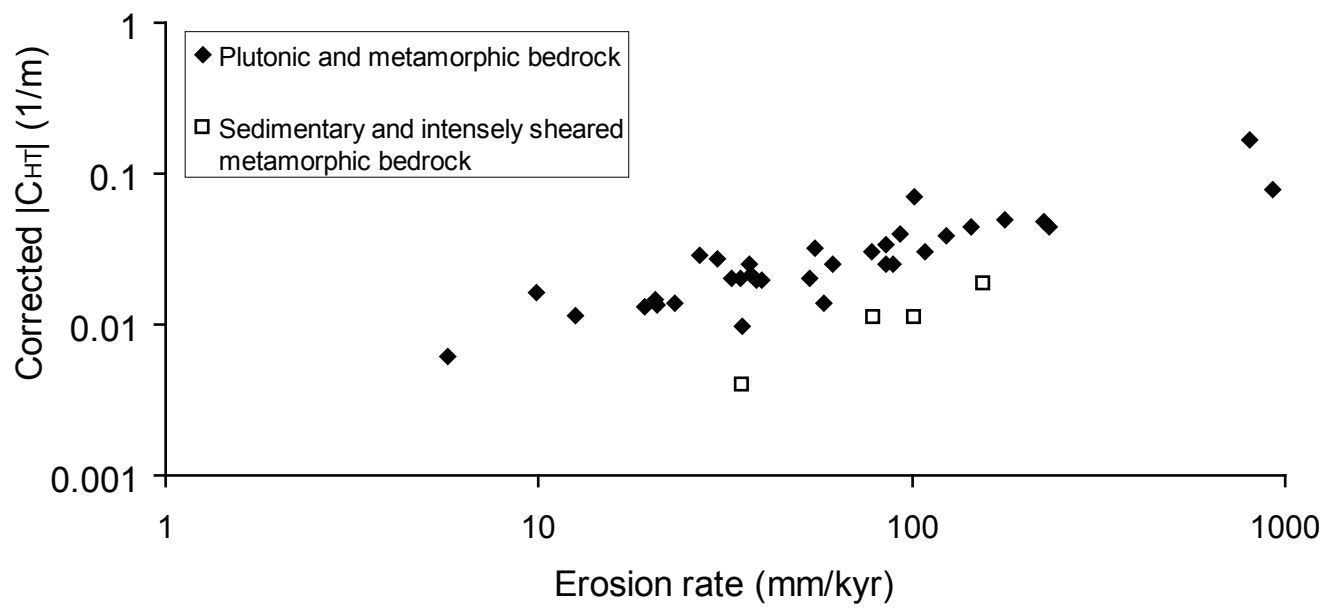


Table 1. Site information. (na = not available)

Region	Source	Sample ID	Latitude (°N)	Longitude (°W)	Lithology <sup>j</sup>	MAT <sup>k</sup> (°C)	MAP <sup>k</sup> (cm/yr)	Eros. ± 1σ (mm/kyr)	Med. Crv. <sup>l</sup> (1/m)	Ave. Slope (m/m)	D <sup>l</sup> ± 1σ (cm <sup>2</sup> /yr)
San Gabriel Mountains (CA)	a	SG128	34.3376	118.0104	gr	12	55.5	37 ± 8	-0.02544	0.031	29 ± 6
	a	SG130	34.3783	117.9893	gr	11	59.8	62 ± 13	-0.02515	0.028	50 ± 10
	a	SG131	34.3666	117.9920	gr	11	58.8	85 ± 20	-0.03410	0.038	49 ± 12
	a	SG132	34.3658	117.9891	gr	11	60.1	93 ± 19	-0.04039	0.043	46 ± 9
	b	na	34.3640	117.9920	gr	na	77.1	108 ± 17	-0.03086	na	70 ± 12
Idaho Plateau (ID)	c	S1	45.4773	114.9618	tnlt	8	62.4	55 ± 11	-0.03254	0.039	34 ± 7
	c	S2	45.5008	114.9519	tnlt	5	71.0	101 ± 21	-0.07189	0.025	28 ± 7
	c	S3	45.5262	114.9293	tnlt	3	116.6	37 ± 7	-0.02139	0.012	34 ± 7
	c	R2	45.4843	114.9558	tnlt	7	61.8	78 ± 16	-0.03083	0.073	51 ± 11
	c	R3	45.5348	114.9015	tnlt	2	119.8	35 ± 7	-0.00971	0.019	72 ± 14
Yucaipa Ridge (CA)	d	3	34.0497	116.9280	qm, gns	9	70.1	922 ± 203	-0.08083	0.092	228 ± 57
	d	4	34.0530	116.9401	qm, gns	9	70.1	801 ± 175	-0.18688	0.159	86 ± 28
Blasingame (CA)	b	na	36.9540	119.6310	tnlt	na	38.7	30 ± 4	-0.02727	na	22 ± 3
Olympic Peninsula (WA)	e	U-WC-S	47.7399	124.0457	gw	8	315.1	177 ± 39	-0.04884	0.049	72 ± 17
	e	L-WC-S	47.7302	124.0379	gw	8	315.1	225 ± 51	-0.04755	0.050	95 ± 22
	e	L-EFMC-S	47.6581	124.2432	gw	9	319.6	144 ± 34	-0.04422	0.049	65 ± 16
Blue Ridge Mountains (VA)	f	SH-01a	38.5713	78.2873	gr	11	107.5	23 ± 5	-0.01391	0.019	33 ± 7
	f	SH-02a	38.6636	78.3550	mb	10	104.5	6 ± 1	-0.00616	0.009	19 ± 4
	f	SH-07	38.5816	78.4144	gr	10	108.6	10 ± 2	-0.01699	0.025	12 ± 2
	f	SH-10	38.6572	78.2822	gr	11	106.8	13 ± 3	-0.01203	0.018	21 ± 5
Feather River (CA)	g	BRB-2	39.6491	121.3020	qd	12	140.0	33 ± 7	-0.02036	0.022	32 ± 7
	h	BEAN-1	39.6126	121.3295	qd	13	133.2	35 ± 8	-0.02013	0.024	35 ± 7
	h	BEAN-2	39.6225	121.3283	qd	14	124.0	38 ± 8	-0.01969	0.024	39 ± 8
	h	BEAN-4	39.6237	121.3273	qd	12	136.1	53 ± 12	-0.02097	0.025	51 ± 11
	h	BEAN-5	39.6312	121.3298	qd	13	136.5	40 ± 8	-0.01954	0.024	40 ± 8
	i	BEAN-7	39.6284	121.3277	qd	13	134.7	85 ± 18	-0.02557	0.030	67 ± 14
	i	FT-3	39.6714	121.3109	qd	11	123.7	21 ± 4	-0.01425	0.017	29 ± 6
	i	FT-4	39.6712	121.3109	qd	11	124.8	21 ± 4	-0.01513	0.020	27 ± 6

	i	FT-6	39.6784	121.3155	qd	10	119.8	19 ± 4	-0.01338	0.017	29 ± 6
	i	SB-1	39.7189	121.2411	qd	8	121.9	58 ± 12	-0.01475	0.019	79 ± 17
	i	FR-4	39.6344	121.2771	qd	15	140.5	234 ± 79	-0.04535	0.035	103 ± 36
	i	FR-5	39.6354	121.2713	qd	15	140.5	124 ± 39	-0.03858	0.047	64 ± 21
Wasatch Mtns (Utah)	b	na	40.8920	111.8650	gr	na	51.5	89 ± 9	-0.02507	na	71 ± 15
Great Smokey Mtns (NC)	b	na	35.6220	83.2040	qtz	na	154.0	27 ± 2	-0.02872	na	19 ± 1

<sup>a</sup> Source for <sup>10</sup>Be data and lithology: [DiBiase *et al.*, 2010]

<sup>b</sup> Source for all data: [Richardson *et al.*, 2019]

<sup>c</sup> Samples were collected for this study; source for lithology: [Wood, 2013]

<sup>d</sup> Source for <sup>10</sup>Be data and lithology: [Binnie *et al.*, 2007]

<sup>e</sup> Source for <sup>10</sup>Be data and lithology: [Belmont *et al.*, 2007]

<sup>f</sup> Source for <sup>10</sup>Be data and lithology: [Duxbury, 2009]

<sup>g</sup> Source for <sup>10</sup>Be data for all Feather River samples except FR-4 and FR-5: [Hurst *et al.*, 2012]

<sup>h</sup> Source for <sup>10</sup>Be data for FR-4 and FR-5: [Riebe *et al.*, 2001]

<sup>i</sup> Source for lithology: [Saucedo and Wagner, 1992]

<sup>j</sup> gr = granitic, tnlt = tonalite, qm = quartz monzonite, gns = gneiss, gw = greywacke, mb = metabasalt, qd = quartz diorite, qtz = quartzite

<sup>k</sup> applies to data from all sources except Richardson *et al.* [2019]; MAT = mean annual temperature; MAP = mean annual precipitation; data from the PRISM Climate Group, <http://prism.oregonstate.edu>, accessed 25 March 2017

<sup>l</sup> Values corrected for grid-resolution effects. Grid-resolution adjustment for sites L-WC-S, L-EFMC-S, SH-01a, SH-02a used a 12-m analysis window because adjustments using 14-window failed to converge to a solution. Sensitivity analyses indicate an average difference of <2% for curvature corrections using a window diameter of 12 m vs. 14 m.

**Table 2.** Details of  $^{10}\text{Be}$  analysis from Idaho site.

Sample ID	Sample depth intervals (cm)	AMS measurement ID	$^{10}\text{Be}$ concentration ( $\times 10^3$ at $\text{g}^{-1}$ )	$^{10}\text{Be}$ concentration uncertainty $1\sigma$ ( $\times 10^3$ at $\text{g}^{-1}$ )
S1	0 - 2	s04446	119.9	5.7
S2	8 - 10	s04447	91.94	7.18
S3	16 - 18	s04448	373.7	17.8
R2	n/a	s04450	91.49	4.43
R3	n/a	s04451	408.8	15.1
R4	n/a	s04452	480.1	16.6